The Astrophysical Journal, 997:71 (10pp), 2026 January 20 https://doi.org/10.3847/1538-4357/ae2b70

Electron Energization in the Evolution of the Kelvin–Helmholtz Instability

Yuhang Yang[1], San Lu[1,2], Quanming Lu[1,2], Ao Guo[1], and Wenya Li[3]
[1] School of Earth and Space Sciences, Deep Space Exploration Laboratory, University of Science and Technology of China, Hefei, People's Republic of China; lusan@ustc.edu.cn, qmlu@ustc.edu.cn
[2] Collaborative Innovation Center of Astronautical Science and Technology, Harbin, People's Republic of China
[3] State Key Laboratory of Solar Activity and Space Weather, National Space Science Center, Chinese Academy of Sciences, Beijing, People's Republic of China
Received 2025 September 15; revised 2025 November 20; accepted 2025 December 5; published 2026 January 14

Abstract

The Kelvin–Helmholtz (K-H) instability is ubiquitous in space and astrophysical environments, playing a vital role in the transport of mass, momentum, and energy. Although it has been shown that the K-H instability can energize the electrons, the mechanisms of electron energization remain unclear. In this paper, two-dimensional full particle-in-cell simulations are used to explore the physical mechanisms governing electron energy variation during the evolution of the K-H instability. By tracking the temporal evolution of electron energy and incorporating the guiding-center theory, we quantitatively analyze the contributions from the parallel electric field, betatron, and Fermi mechanisms to electron energization. The results demonstrate that as the instability develops, vortices roll up and expand, with electron energization dominated by the betatron mechanism. Subsequently, small-scale magnetic reconnection disrupts the vortices, and the parallel electric field becomes the primary driver of electron energization. The vortices eventually merge into a larger vortex, and the betatron mechanism regains dominance due to the roll-up of the large-scale vortex. The Fermi mechanism contributes minimally to electron energization and even exhibits a cooling effect during vortices' expansion. This study elucidates the primary pathways of electron energization during the K-H instability evolution, providing theoretical insights into energy dissipation mechanisms in magnetized plasmas under velocity shear conditions.

Unified Astronomy Thesaurus concepts: Plasma physics (2089); Space plasmas (1544); Solar energetic particles (1491)

Materials only available in the online version of record: animation

1. Introduction

The Kelvin–Helmholtz (K-H) instability is a shear-driven interfacial instability that occurs in both fluid and plasma systems when the velocity gradient exceeds a critical threshold (S. Chandrasekhar 1961; A. Miura & P. L. Pritchett 1982; Z. Pu & M. G. Kivelson 1983; J. R. Johnson et al. 2014; T. K. M. Nakamura et al. 2022). As the instability evolves into the nonlinear stage, vortices emerge at the interface, which represent a key characteristic of the K-H instability (A. Miura 1984). The instability is ubiquitous in space and astrophysical plasmas, such as the flanks of Earth's and planetary magnetopauses (H. Hasegawa et al. 2004; J. Paral & R. Rankin 2013; W. Li et al. 2016; S. Lu et al. 2025), the boundaries of coronal mass ejections (K. Nykyri & C. Foullon 2013), the heliopause boundary (C. Wang & J. W. Belcher 1998), the atmosphere of Jupiter (S. Fromang et al. 2016), the pulsar wind (N. Bucciantini et al. 2020), and the astrophysical jets (F. M. Rieger & P. Duffy 2004). The K-H instability occurring at the Earth's low-latitude magnetopause flank is widely recognized as a key mechanism for cross-boundary transport of mass, momentum, and energy of the plasma between the solar wind and the magnetosphere (K. Nykyri & A. Otto 2001; H. Hasegawa et al. 2004; T. K. M. Nakamura et al. 2017).

Beyond the plasma transport, the K-H instability plays a critical role in electron energization. Both observations (W. Li et al. 2016; K.-J. Hwang et al. 2020) and simulations (T. K. M. Nakamura et al. 2011, 2017) provide evidence for this process. How electrons gain energy within vortices has been explored in several studies. Kinetic simulations demonstrate that K-H vortices roll up and saturate, resulting in turbulence, which cascades to form small-scale current sheets. The current sheets produce intense localized electron heating through their embedded parallel electric field (M. Wan et al. 2012; H. Karimabadi et al. 2013), with heating linked strongly to electron vorticity structures (J. Goodwill et al. 2025). More recently, the K-H instability has been observed in large-scale magnetic islands formed during reconnection, where secondary reconnection events occur, heating electrons near reconnection sites (C. Huang et al. 2015, 2017; Q. Lu et al. 2023; K. Jiang et al. 2025). Recent in situ observations reveal that energetic electrons can be generated inside an ion flow vortex, where their acceleration is achieved through the establishment of the Fermi acceleration trap and the parallel electrostatic potential (C. M. Liu et al. 2025). Although these studies have demonstrated that the K-H instability can energize electrons, which process or processes are the primary drivers of electron energization remains an open question. Therefore, it is essential to quantitatively analyze the mechanisms by which electrons gain energy within K-H vortices.

According to the linear theory by S. Chandrasekhar (1961), the magnetic field component parallel to the propagation direction of K-H waves tends to stabilize the instability. When the magnetic field direction is almost perpendicular to the shearing flow direction, the instability condition is more readily satisfied. Under such conditions, electrons remain almost magnetized and show adiabatic behavior, thus making the guiding-center theory reasonable, which describes particle acceleration via the parallel electric field, betatron, and Fermi mechanisms (T. G. Northrop 1963). Previous studies have

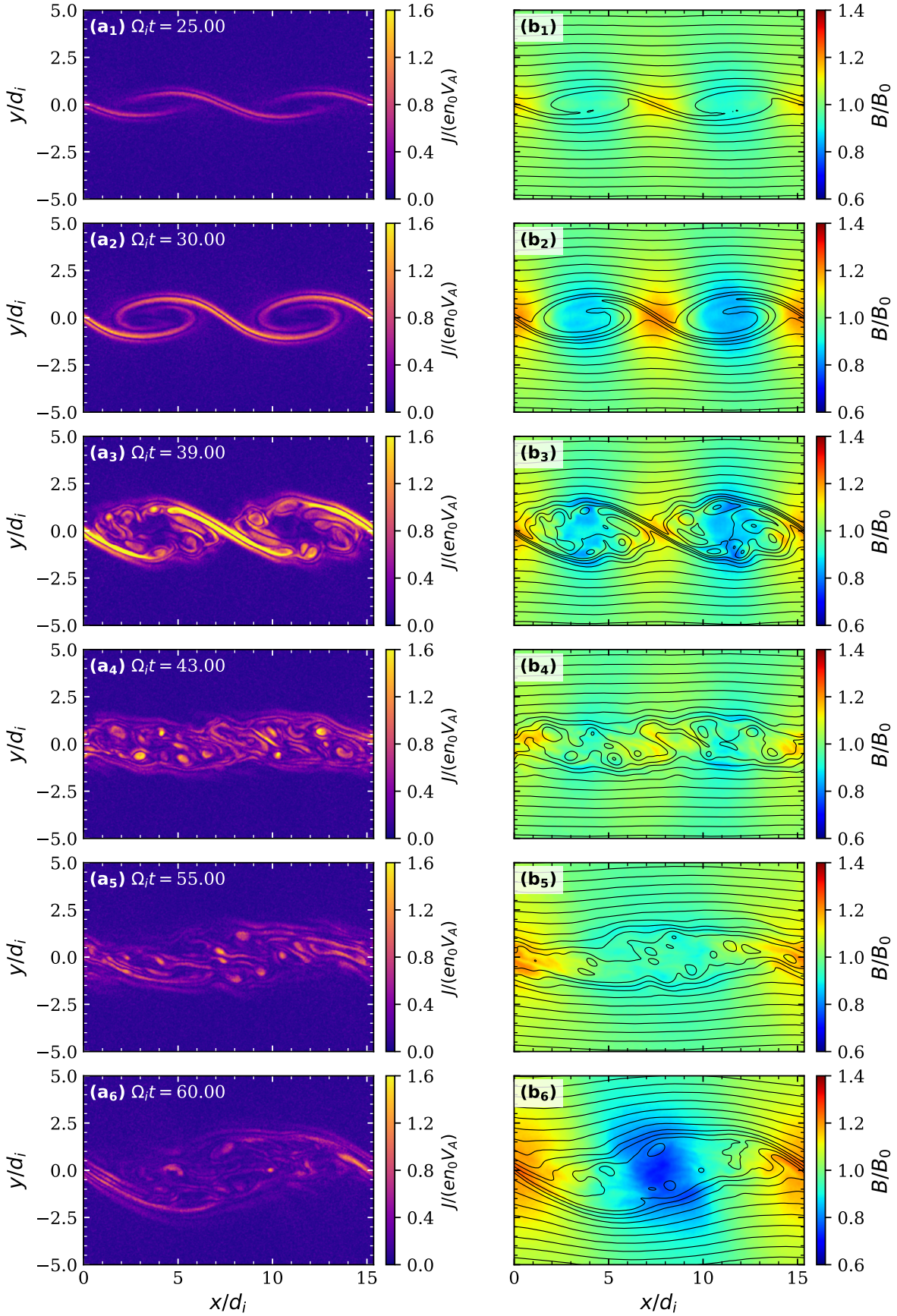

Figure 1. The temporal evolution of the spatial distribution of total current density $J/(en_0V_A)$ and magnetic field strength B/B_0 at $\Omega_i t$= 25, 30, 39, 43, 55, and 60. Magnetic field lines, depicted by black solid curves in panels (b_1)–(b_6), illustrate the topology of the field. A 30 s animation of this figure is available in the online journal. (An animation of this figure is available in the online article.)

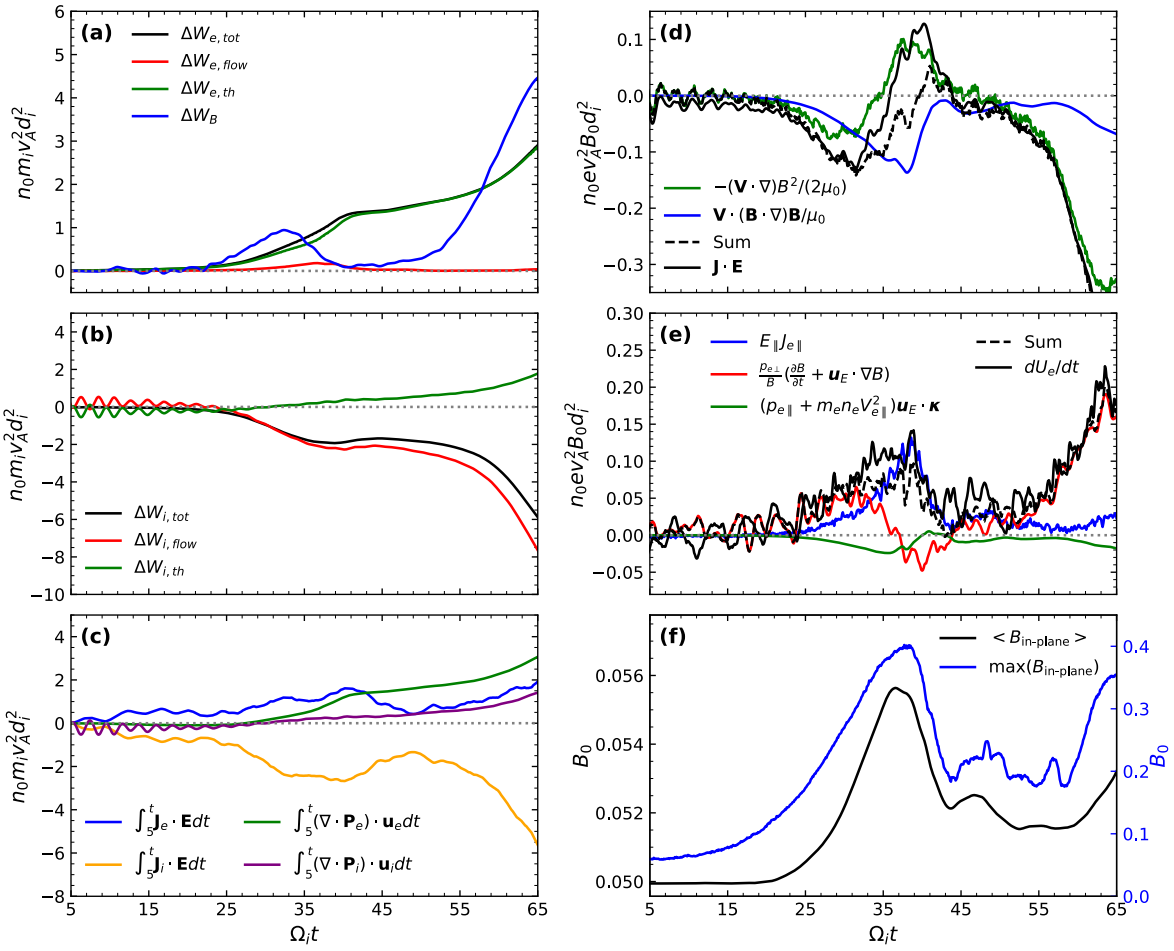

Figure 2. Time evolution of (a) relative changes in electron total energy, kinetic flow energy, thermal energy, and magnetic field energy; (b) relative changes in ion total energy, kinetic flow energy, and thermal energy; (c) work done to electrons and ions by electric field and pressure gradient force, which are integrated over the simulation box; (d) power of magnetic pressure gradient, power of magnetic tension force, their sum, and the term $\boldsymbol{J} \cdot \boldsymbol{E}$, which are integrated over the simulation box; (e) the contributions of the parallel electric field, betatron, and Fermi mechanisms to electron energization, which is calculated from Equation (5); and (f) the mean value $\langle B_{\text{in-plane}} \rangle$ and the maximum value $\max(B_{\text{in-plane}})$ of the in-plane magnetic field strength.

quantitatively analyzed the contributions of these mechanisms to electron energization during magnetic reconnection with a guide field by summing over all electrons within the simulation domain (J. T. Dahlin et al. 2014; H. Wang et al. 2016; Q. Lu et al. 2018). In this study, using two-dimensional particle-in-cell (PIC) simulations, we investigate electron energization mechanisms with the guiding-center theory during the K-H instability evolution. We follow the temporal evolution of various energy components and examine the contributions from various mechanisms to electron energization at different stages of the instability.

2. Simulation Model

An open-source PIC code named Smilei is employed in this paper to perform the two-dimensional simulations of the K-H instability in the x–y plane (J. Derouillat et al. 2018). Particles are confined to two-dimensional space, while their velocities and associated fields remain three-dimensional. The magnetic field $\boldsymbol{B} = B_0 \sin\theta \boldsymbol{e}_x + B_0 \cos\theta \boldsymbol{e}_z$ is uniform, where B_0 is the magnetic field intensity and $\theta = 2.86^\circ$ is the inclination angle of the magnetic field relative to the z-direction, with the out-of-plane component being approximately 20 times stronger than the in-plane component. The distribution function of each species is a drifting Maxwellian with a uniform temperature T_0 and drift velocity $\boldsymbol{V} = V_0 \tanh((y - y_0)/\delta)\boldsymbol{e}_x$, where $V_0 = -20V_A^*$ ($V_A^* = B_0 \sin\theta/\sqrt{\mu_0 n_0 m_i}$ is the in-plane Alfvén speed) and $\delta = 0.4d_i$ is the half-width of the shear layer ($d_i = c/\omega_{pi}$ is the ion inertial length based on the plasma density n_0). In order to sustain the shear flow, we impose an electric field $\boldsymbol{E} = V_0 B_0 \cos\theta \tanh((y - y_0)/d)\boldsymbol{e}_y$ and initialize the electron density with a slight nonuniformity to satisfy Gauss's law. In order to initiate the K-H instability, a small velocity perturbation of the form $\delta V_{iy} = \delta V_{ey} = \delta V_0 \cdot V_0 \sin(2\pi x/L_x) \exp[-(y - y_0)^2/d^2]$ is introduced at the initial time, where $\delta V_0 = 0.01$ represents the perturbation amplitude.

The system size is $L_x \times L_y = 15.36d_i \times 30.72d_i$, and a uniform computational grid with 1536×3072 cells is employed, resulting in a cell size of approximately 0.95 Debye length. The average number of particles per cell is 100, and about 4.8×10^8 particles for each species are used in our simulation. The time step is $\Omega_i \Delta t \approx 1.7 \times 10^{-4}$, where Ω_i is the ion gyrofrequency. The ion-to-electron mass ratio is set at $m_i/m_e = 100$, the speed of light is $c = 30V_A$ (V_A is the Alfvén speed defined by $V_A = B_0/\sqrt{\mu_0 n_0 m_i}$), and the plasma beta values of ion and electron are $\beta_i = \beta_e = 0.4$. Periodic boundary conditions are applied to electromagnetic fields and particles in the x-direction, while perfectly conducting

boundary conditions for electromagnetic fields and reflective boundary conditions for particles are used in the y-direction.

Our initial condition is similar to those used in previous simulation studies (M. Wan et al. 2012; H. Karimabadi et al. 2013; J. Goodwill et al. 2025), and this setup is representative for many astrophysical plasma environments, such as Earth's and planetary magnetopause boundaries (J. Paral & R. Rankin 2013; A. Settino et al. 2024), the solar wind (R. Kieokaew et al. 2021), and coronal mass ejection boundaries (K. Nykyri & C. Foullon 2013; E. Paouris et al. 2024). In these environments, flow shear is the dominant driver, while magnetic shear is relatively weak. The magnetic and thermal pressures are comparable, with plasma beta typically ranging from 0.1 to 10. In addition, a magnetic field component perpendicular to the shear flow plane is often present, which acts as a guide field for in-plane magnetic reconnection during the evolution of the K-H instability. The scale perpendicular to the shear flow plane is large, and within the scope of our simulation, physical quantities in the z-direction remain nearly unchanged, allowing us to treat this direction as uniform.

3. Results

The spatial evolution of the total current density and magnetic field structure is shown in Figure 1 at $\Omega_i t = 25$, 30, 39, 43, 55, and 60 (an animation of this figure is available). As the K-H instability develops, two vortices roll up. During the subsequent vortex evolution, the continuous roll-up and expansion of vortical structures occur simultaneously with stretching of magnetic field lines, and the magnetic field becomes weakened within vortices but intensified in the area between two vortices. This roll-up process generates current sheets. The system reaches a stage at $\Omega_i t = 39$ when these current sheets are compressed down to electron inertial lengths. This compression triggers tearing instabilities at multiple discrete locations along the sheets, initiating magnetic reconnection that produces a chain of magnetic islands. Subsequently, the vortices break into smaller structures, disrupting the original magnetic field configuration and transitioning the system into a turbulent state. At $\Omega_i t = 60$, a larger vortex gradually emerges, culminating in vortex merging.

To analyze the system's evolution process and the mechanisms of electron energization, we calculate the variations of several energy components and corresponding energy transfer, as well as the contributions of the mechanisms to electron energy enhancement within the simulation box. In plasmas, the total energy can be decomposed into electromagnetic, species flow kinetic, and species thermal components, between which energy transfer occurs. The energy conversion equations can be written as follows:

$$\frac{\partial}{\partial t}\left(\frac{B^2}{2\mu_0}\right) = -\nabla \cdot \boldsymbol{S} - \boldsymbol{J} \cdot \boldsymbol{E}, \tag{1}$$

$$\frac{\partial U_{s,\mathrm{flow}}}{\partial t} = -\nabla \cdot (U_{s,\mathrm{flow}} \boldsymbol{V}_s) + \boldsymbol{J}_s \cdot \boldsymbol{E} - \left(\nabla \cdot \ddot{\boldsymbol{P}}_s\right) \cdot \boldsymbol{V}_s, \tag{2}$$

$$\frac{\partial U_{s,\mathrm{th}}}{\partial t} = -\nabla \cdot \boldsymbol{H}_s - \nabla \cdot \boldsymbol{q}_s + \left(\nabla \cdot \ddot{\boldsymbol{P}}_s\right) \cdot \boldsymbol{V}_s. \tag{3}$$

Here $s = i, e$ denotes the particle species, $B^2/(2\mu_0)$ is the magnetic energy, $U_{s,\mathrm{flow}}$ is the flow kinetic energy, $U_{s,\mathrm{th}}$ is the thermal energy, $\boldsymbol{J}$ is the current density, $\boldsymbol{E}$ is the electric field, $\boldsymbol{V}$ is the flow velocity, $\ddot{\boldsymbol{P}}_s$ is the pressure tensor, $\boldsymbol{S} = (\boldsymbol{E} \times \boldsymbol{B})/\mu_0$ is the Poynting vector, $\boldsymbol{H}_s = U_{s,\mathrm{th}} \boldsymbol{V}_s + \ddot{\boldsymbol{P}}_s \cdot \boldsymbol{V}_s$ is the enthalpy flux, and $\boldsymbol{q}_s$ is the heat flux. The term $\boldsymbol{J} \cdot \boldsymbol{E}$ represents the conversion between magnetic energy and fluid kinetic energy, and $(\nabla \cdot \ddot{\boldsymbol{P}}) \cdot \boldsymbol{V}$ governs the conversion between flow kinetic energy and thermal energy. When integrated over the simulation box, the transport terms are zero in the closed system. To eliminate initial fluctuations associated with numerical settings in the system, the calculated energy variations are normalized to the reference time at $\Omega_i t = 5$. Figures 2(a)–(c) depict the temporal evolution of the total electron and ion energies, flow kinetic energy, thermal energy, magnetic field energy, and the time-integrated energy transfer among these components. When the instability develops into the nonlinear phase around $\Omega_i t = 25$, the ion flow kinetic energy begins to decrease rapidly, while the magnetic energy, electron thermal energy, and ion thermal energy increase. Throughout the simulation, ion flow energy is converted into other forms of energy, most notably into electron thermal energy.

Note that the term $\boldsymbol{J} \cdot \boldsymbol{E}$ is mostly contributed by the work done by the Lorentz force, and the Lorentz force consists of the magnetic pressure gradient and the magnetic tension. To better understand the conversion between fluid energy and magnetic energy, Figure 2(d) displays the time evolution of the power of the magnetic pressure gradient, the power of the magnetic tension force, their sum, and the term $\boldsymbol{J} \cdot \boldsymbol{E}$, which are integrated over the simulation box. The work done by the Lorentz force, $\boldsymbol{V} \cdot (\boldsymbol{J} \times \boldsymbol{B})$, can be rewritten as the sum of the work done by the magnetic pressure gradient and the work done by the magnetic tension force (A. Beresnyak & H. Li 2016; J. T. Dahlin et al. 2017):

$$\boldsymbol{V} \cdot (\boldsymbol{J} \times \boldsymbol{B}) = -\frac{(\boldsymbol{V} \cdot \nabla) B^2}{2\mu_0} + \frac{\boldsymbol{V} \cdot (\boldsymbol{B} \cdot \nabla) \boldsymbol{B}}{\mu_0}. \tag{4}$$

Here $\boldsymbol{V} \cdot (\boldsymbol{J} \times \boldsymbol{B})$ is the power density of the Lorentz force, $-(\boldsymbol{V} \cdot \nabla) B^2/(2\mu_0)$ represents the power density of the magnetic pressure gradient, and $\boldsymbol{V} \cdot (\boldsymbol{B} \cdot \nabla) \boldsymbol{B}/\mu_0$ denotes the power density of the magnetic tension. As the vortices roll up, both the magnetic tension force and the magnetic pressure gradient perform negative work, with their magnitudes being comparable, thereby converting fluid energy into magnetic energy. During the stage where the vortices break up, the power associated with these forces progressively weakens, leading to a decrease in the efficiency of energy conversion.

We then investigate the electron energization. In our simulations, the magnetic field is primarily oriented out of plane, and electrons can be considered adiabatic. Thus, the guiding-center theory can be employed to analyze electron acceleration and heating in the instability, which is verified by the subsequent results. The total electron energy is governed by the following equation (T. G. Northrop 1963; J. T. Dahlin et al. 2014; H. Wang et al. 2016; Q. Lu et al. 2018):

$$\frac{dU_e}{dt} = E_{\parallel} J_{e\parallel} + \frac{p_{e\perp}}{B}\left(\frac{\partial B}{\partial t} + \boldsymbol{u}_E \cdot \nabla B\right) + \left(p_{e\parallel} + m_e n_e V_{e\parallel}^2\right) \boldsymbol{u}_E \cdot \boldsymbol{\kappa}, \tag{5}$$

where U_e is the total electron energy, $E_{\parallel}$ denotes the electric field component parallel to the magnetic field, $J_{e\parallel}$ represents the parallel electron current, B is the magnetic field strength,

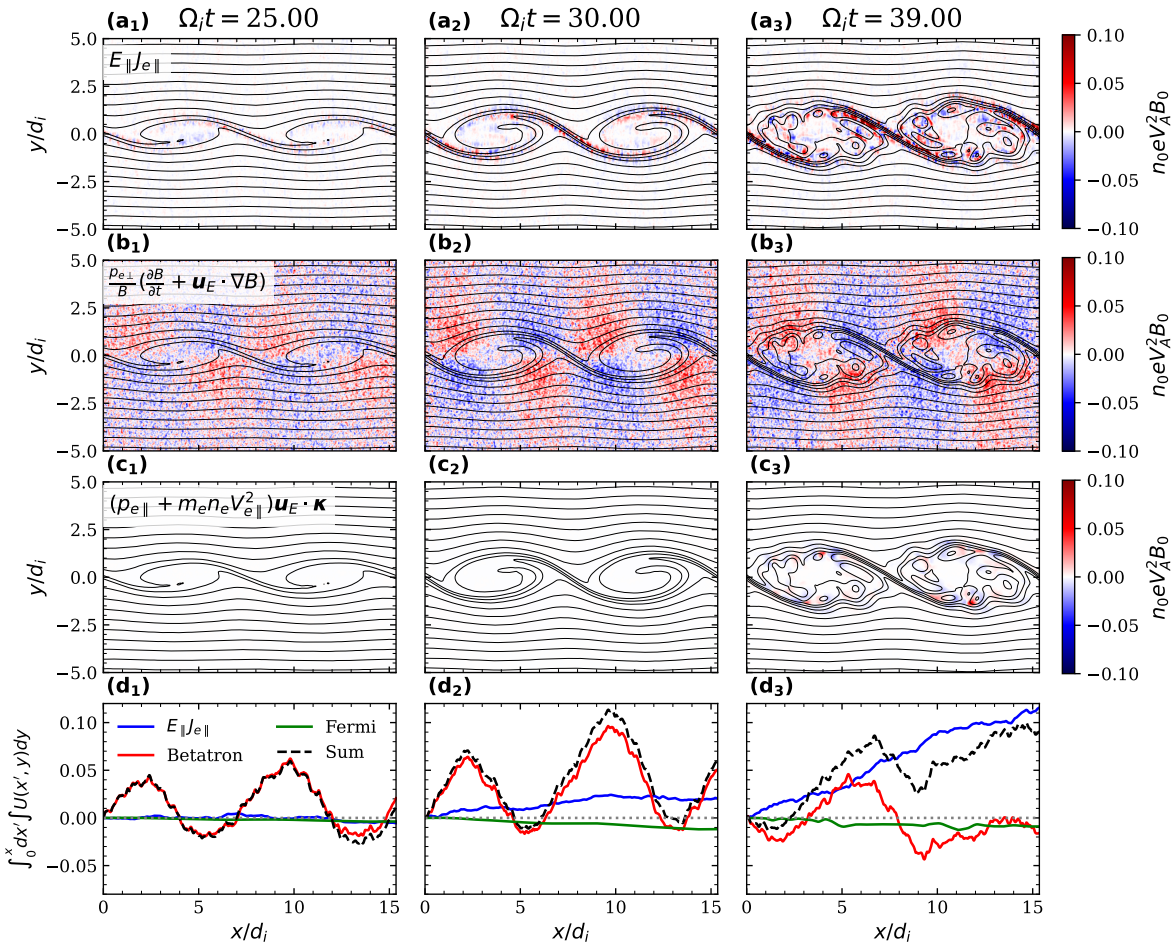

Figure 3. The panels display, from top to bottom: the spatial distributions of electron energization contributions from the parallel electric field, betatron, and Fermi mechanisms at $\Omega_i t$= 25, 30, and 39, along with their spatially integrated values $\int_0^x dx' \int U(x', y)dy$ (here, $U(x', y)$ is the term contributed by either the parallel electric field, betatron, or Fermi mechanisms).

m_e is the electron mass, n_e is the electron number density, $V_{e\|}$ is the parallel electron bulk velocity, $p_{e\perp}$ and $p_{e\|}$ are the perpendicular and parallel electron pressures, $\boldsymbol{u}_E = (\boldsymbol{E} \times \boldsymbol{B})/B^2$ is the "$\boldsymbol{E} \times \boldsymbol{B}$" drift, and $\boldsymbol{\kappa} = \boldsymbol{b} \cdot \nabla \boldsymbol{b}$ (where $\boldsymbol{b} = \boldsymbol{B}/B$) is the magnetic field curvature. The first term represents electron acceleration by the parallel electric field, the second term corresponds to betatron heating/cooling, and the final term relates to first-order Fermi acceleration. Figure 2(e) presents the contributions from the parallel electric field, betatron, and Fermi mechanisms to electron energy gain, as calculated by Equation (5). Notably, the rate of electron energy change, dU_e/dt, closely matches the sum of the three terms, indicating that the guiding-center theory accurately describes the electron energy variation rate. The difference between dU_e/dt and the sum arises from nonadiabatic motion of some electrons, which can be driven by the thin current sheets formed at vortex edges and cannot be described by the guiding-center theory (K. Steinvall et al. 2025). Figure 2(f) illustrates the temporal evolution of both the mean value $\langle B_{\text{in-plane}} \rangle$ and maximum value $\max(B_{\text{in-plane}})$ of the in-plane magnetic field. Up to approximately $\Omega_i t = 36$, $\langle B_{\text{in-plane}} \rangle$ gradually increases to about 0.055 B_0, with the maximum value reaching about 0.4 B_0. Subsequently, as the vortices gradually break down, $\langle B_{\text{in-plane}} \rangle$ decreases to about 0.052 B_0, and the maximum value drops to about 0.2 B_0. The electron energization process can be divided into three stages. In the first stage (approximately from $\Omega_i t = 25$ to 36), K-H vortices roll up, expand, and distort magnetic field lines, converting shear flow energy into magnetic energy. The magnetic field accumulates, and electron energization is primarily driven by the betatron mechanism. In the second stage (approximately from $\Omega_i t = 36$ to 50), magnetic reconnection annihilates the antiparallel in-plane magnetic field, returning magnetic energy to the plasma. The vortices gradually break down into a turbulent state, suppressing further vortex roll-up and expansion, during which the parallel electric field plays the dominant role. In the third stage (approximately from $\Omega_i t = 50$ to 65), a larger vortex grows on the broadened shear layer, and the K-H vortex rolls up and expands again, with the betatron mechanism effect regaining dominance. Throughout these stages, the effect of the Fermi mechanism is small, which can be attributed to the weak in-plane magnetic field or the dominant guide field in our system (J. T. Dahlin et al. 2016; X. Li et al. 2019; H. Arnold et al. 2021). During vortices' expansion, it becomes negative.

In Figures 3 and 4, we present from top to bottom the spatial distributions of the contributions from the parallel electric field,

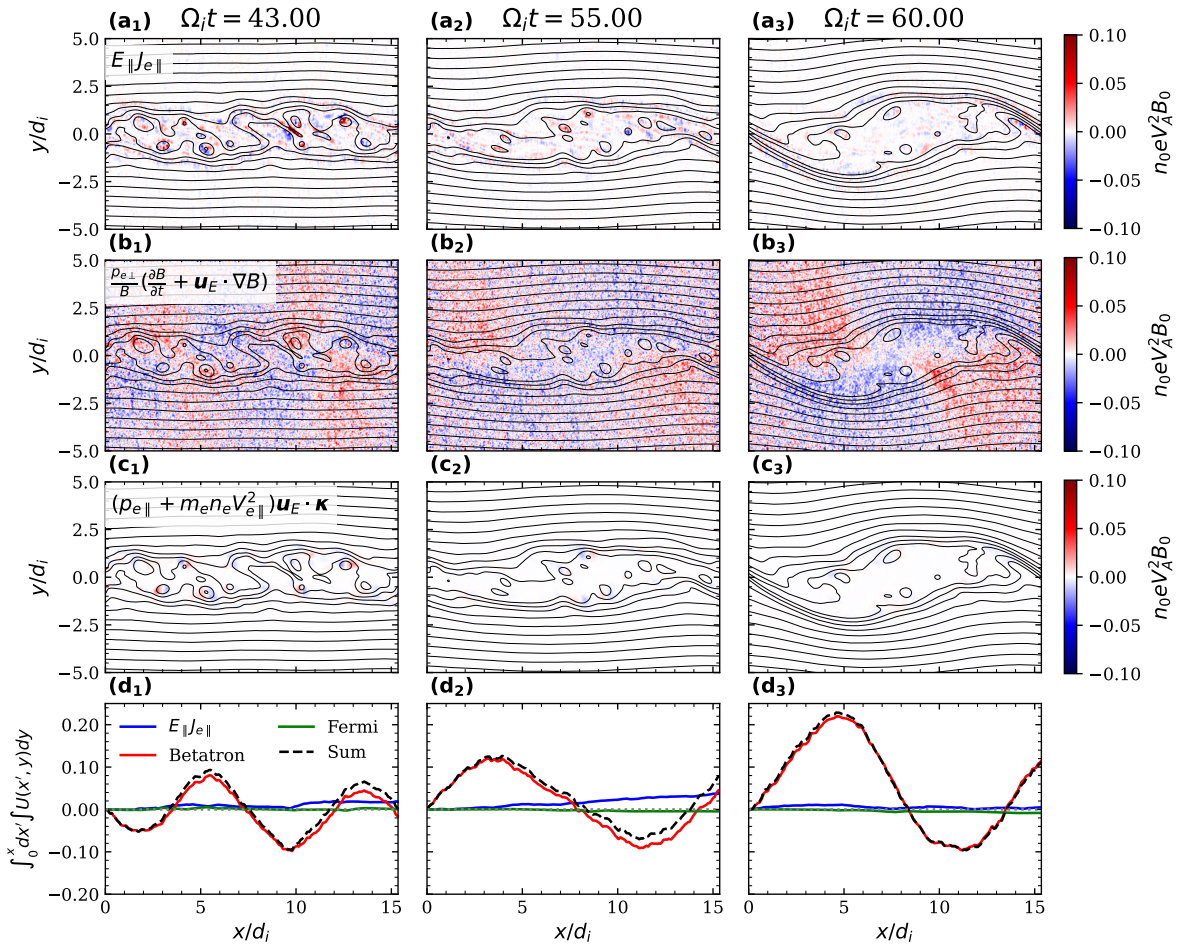

Figure 4. Similar to Figure 3, the spatial distributions of electron energization contributions from the parallel electric field, betatron, and Fermi mechanisms at $\Omega_i t$= 43, 55, and 60, along with their spatially integrated values.

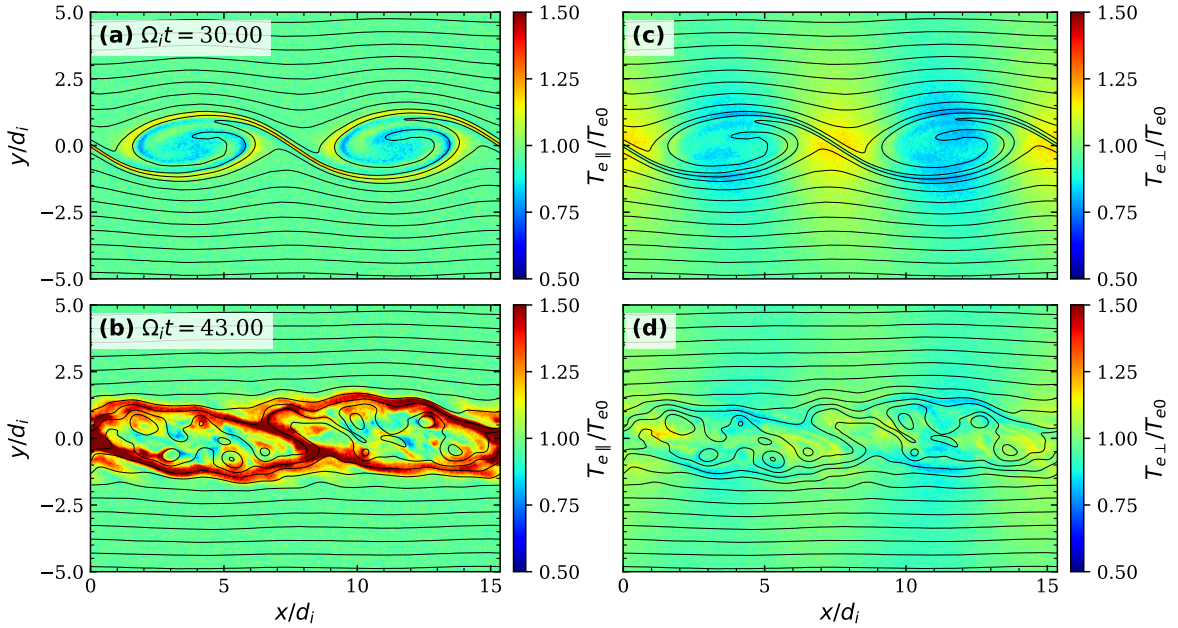

Figure 5. The spatial distribution of (a), (b) electron parallel temperature $T_{e\parallel}/T_{e0}$ and (c), (d) perpendicular temperature $T_{e\perp}/T_{e0}$ at $\Omega_i t$ = 30 and 43, normalized by initial temperature T_{e0} (here, T_{e0} represents the initial electron temperature, assumed isotropic).

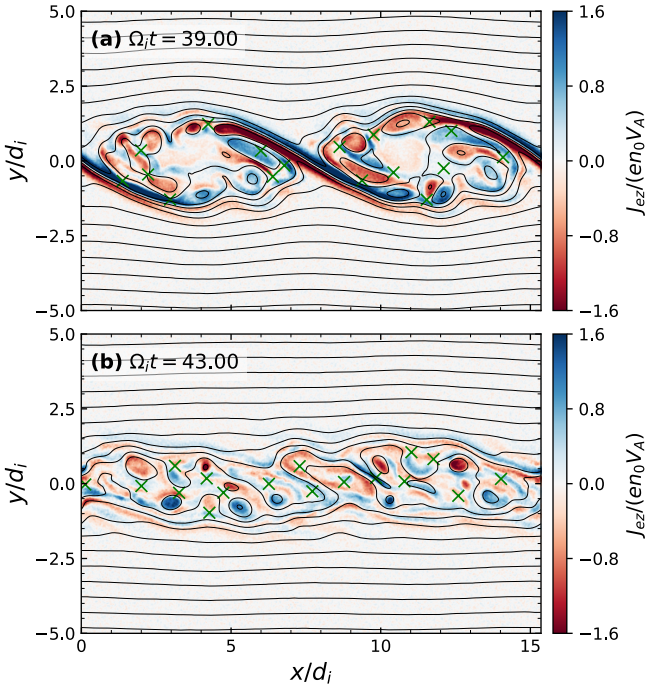

Figure 6. Spatial distribution of identified X-lines at $\Omega_i t = 39$ and 43. Identified X-lines (green "x") are marked on the in-plane magnetic field line (black line). The color indicates the electron current in the z-direction.

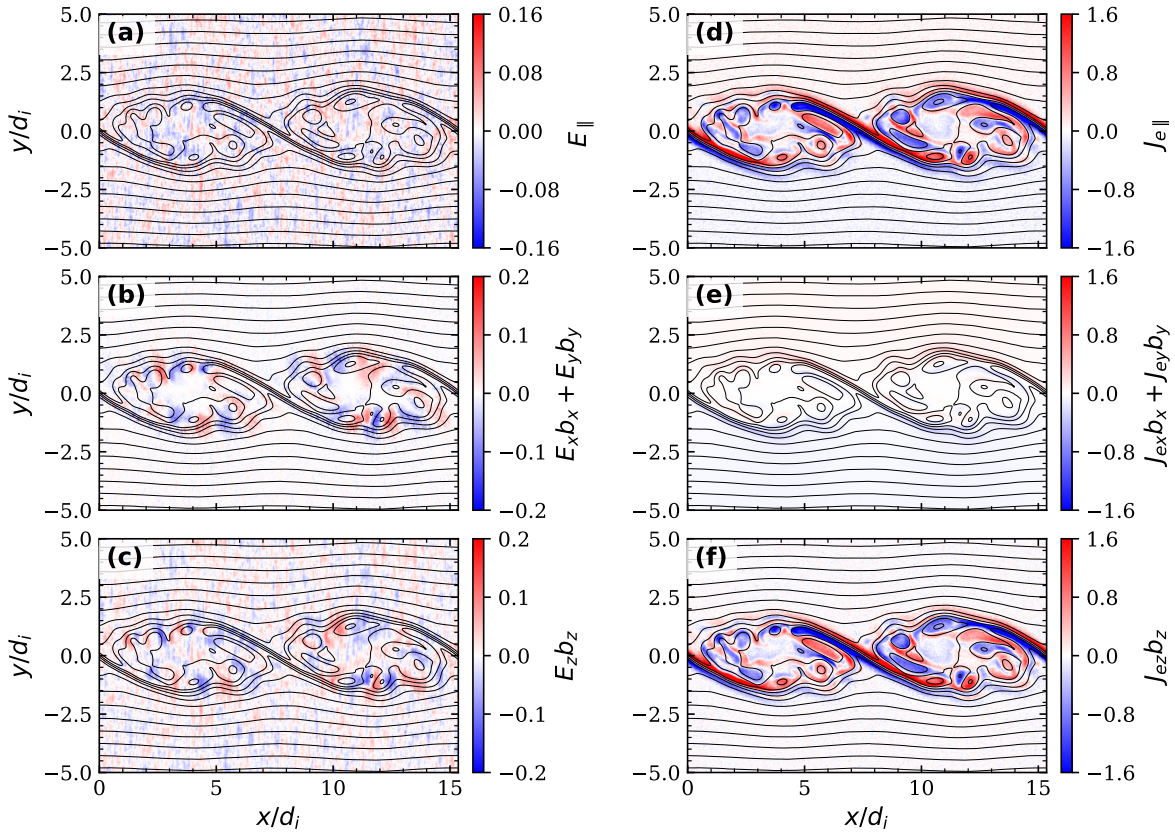

Figure 7. (a) Parallel electric field $E_\parallel = E_x b_x + E_y b_y + E_z b_z$, where $\boldsymbol{b} = \boldsymbol{B}/B$, (b) in-plane component $E_x b_x + E_y b_y$, (c) out-of-plane component $E_z b_z$, (d) parallel electron current $J_{e\parallel} = J_{ex} b_x + J_{ey} b_y + J_{ez} b_z$, (e) in-plane component $J_{ex} b_x + J_{ey} b_y$, (f) out-of-plane component $J_{ez} b_z$ at $\Omega_i t = 39$. The black lines represent the in-plane magnetic field lines.

betatron, and Fermi mechanisms to electron energization at $\Omega_i t = 25$, 30, 39, 43, 55, and 60, along with their corresponding spatially integrated contributions $\int_0^x dx' \int U(x', y) dy$. Here, $U(x', y)$ represents one of the parallel electric field, betatron, or Fermi mechanisms, where the slope indicates the electron energization contribution at a given x. At $\Omega_i t = 25$ and 30, the figures illustrate the process of the K-H vortices' roll-up,

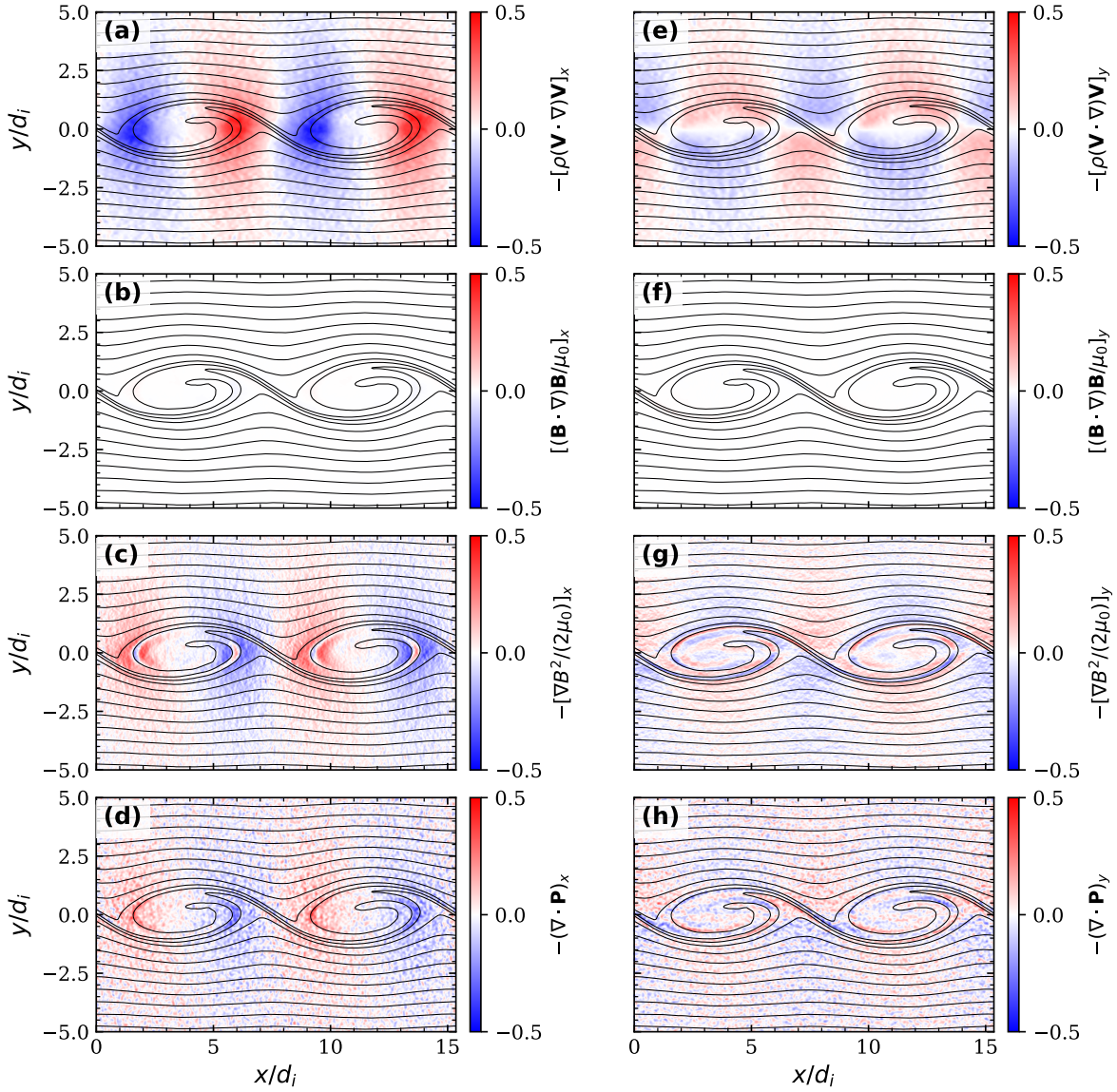

Figure 8. The inertial force $-\rho(\boldsymbol{V}\cdot\nabla)\boldsymbol{V}$, the magnetic tension force $(\boldsymbol{B}\cdot\nabla)\boldsymbol{B}/\mu_0$, the magnetic pressure gradient $-\nabla B^2/(2\mu_0)$, and the thermal pressure gradient $-\nabla\cdot\ddot{\boldsymbol{P}}$ in the x- and y-directions at $\Omega_i t = 30$. The black lines represent the in-plane magnetic field lines.

expansion, and magnetic field line distortion. During this phase, electron energization is primarily driven by the betatron mechanism. Within a K-H vortex, the betatron contribution exhibits a quadrupolar structure in its spatial distribution, which arises from the nonuniform magnetic field structure shown in Figure 1. As electrons flow, they experience varying magnetic field strength, resulting in betatron heating in two quadrants and deceleration in the other two, thereby naturally creating the observed quadrupolar structure. The magnetic field is weaker at the vortex center and stronger between two vortices, resulting in cooling of electrons at the vortex center and heating between vortices. The contributions from both the parallel electric field and Fermi mechanism are relatively small, with the net effect of the parallel electric field being electron energization, while the Fermi mechanism causes electron cooling. At $\Omega_i t = 39$, when multiple magnetic islands form within the vortices, the system is in a reconnection-active phase. Here, electrons are primarily accelerated by the parallel electric field, mainly at the vortex edges, with a net positive contribution. As the original magnetic field structure becomes disrupted, the betatron mechanism becomes less significant. By $\Omega_i t = 43$, the vortices break up and transition into a turbulent state, with electron energization now dominated by both the parallel electric field and the betatron mechanism. Finally, at $\Omega_i t = 60$, the panels show the roll-up of a larger-scale K-H vortex, during which the betatron mechanism regains dominance in electron energization.

Figure 5 shows the spatial distributions of the parallel temperature $T_{e\parallel}$ and perpendicular temperature $T_{e\perp}$ at $\Omega_i t = 30$ and 43, normalized to the initial temperature T_{e0}. The parallel electron temperature decreases at the vortex center but increases at the vortex edges. Similarly, the perpendicular temperature decreases within the vortex center but increases in the areas between vortices. Therefore, electron energization along the magnetic field direction is associated with the parallel electric field, whereas energization perpendicular to the magnetic field is mainly governed by the betatron mechanism.

To investigate the role of magnetic reconnection in electron energization, we identify the locations of each reconnection site. A method commonly used for saddle point identification in two-dimensional turbulent plasmas is employed

(C. C. Haggerty et al. 2017; A. Guo et al. 2023). First, we locate magnetic null points (where $B_p \approx 0$, with B_p being the in-plane magnetic field strength) in the simulation plane. Then, we compute the Hessian matrix $H_{i,j} = \dfrac{\partial^2 a}{\partial x \partial y}$ (where a is the magnetic vector potential of the in-plane field) at each null point and its eigenvalues. If the product of the eigenvalues at a magnetic null point is negative, then it constitutes a saddle point, specifically an X-line. Due to noise in PIC simulations at Debye length scales, which leads to significant overestimation of null points, we employ a density-based clustering algorithm to address this numerical issue (G. Lapenta et al. 2022). If multiple X-lines are separated by distances less than $5d_{e0}$, they are grouped into a single X-line cluster. Each cluster is then replaced by a single point at the average position of its constituent points. Figure 6 shows the locations of the identified X-lines at $\Omega_i t = 39$ and 43. At $\Omega_i t = 39$, X-lines are primarily distributed along the edges of vortices. By $\Omega_i t = 43$, they become more fragmented and scattered throughout the vortices. In Figure 7, we plot the parallel electric field $E_\parallel = E_x b_x + E_y b_y + E_z b_z$, its in-plane component $E_x b_x + E_y b_y$, out-of-plane component $E_z b_z$, parallel electron current $J_{e\parallel} = J_{ex} b_x + J_{ey} b_y + J_{ez} b_z$, in-plane component $J_{ex} b_x + J_{ey} b_y$, and out-of-plane component $J_{ez} b_z$ at $\Omega_i t = 39$. We find that the parallel electric field exhibits a turbulent distribution across the plane, while the parallel current, which is primarily contributed by the out-of-plane component, is predominantly localized at the vortex edge and around the formed magnetic islands. In guide-field reconnection simulations, the parallel electric field comprises both electrostatic and electromagnetic components (S. Lu et al. 2021; S. Hu et al. 2025). The electrostatic component of the parallel electric field is primarily contributed by the Hall electric field, while its electromagnetic component mainly originates from the reconnection electric field. Specifically, the parallel electric field is dominated by the reconnection electric field in the electron inflow region and the Hall electric field in the electron outflow region. These two components largely cancel each other in other parts of the reconnection region. In our simulation, the guide field is very strong, with the magnetic field predominantly oriented in the out-of-plane direction. Near the X-lines, both in-plane and out-of-plane components of the parallel electric field exhibit significant strength, though their effects largely cancel over extended spatial domains. Notably, X-lines and the parallel electric field do not show a strict spatial correspondence, since the parallel electric field is not confined solely to the vicinity of X-lines but can also appear in other regions (primarily the out-of-plane component). Consequently, the generation of the parallel electric field in the K-H vortices shows some connection with magnetic reconnection, though their precise correlation requires further investigation in future studies.

To better understand why the magnetic field increases between the vortices but decreases inside them in Figure 1, we conduct an analysis of the forces acting. Assuming the vortex structure is in a steady state, the force balance equation is given by

$$-\rho(\boldsymbol{V}\cdot\nabla)\boldsymbol{V} + \frac{(\boldsymbol{B}\cdot\nabla)\boldsymbol{B}}{\mu_0} - \nabla\left(\frac{B^2}{2\mu_0}\right) - \nabla\cdot\vec{\boldsymbol{P}} = 0. \quad (6)$$

Here $-\rho(\boldsymbol{V}\cdot\nabla)\boldsymbol{V}$ represents the inertial force, $(\boldsymbol{B}\cdot\nabla)\boldsymbol{B}/\mu_0$ denotes the magnetic tension force, $-\nabla B^2/(2\mu_0)$ is the magnetic pressure gradient, and $-\nabla\cdot\vec{\boldsymbol{P}}$ corresponds to the thermal pressure gradient. When vortices form, the inertial force increases and points outward from the vortex center, compressing the areas between vortices. Simultaneously, the magnetic tension force, magnetic pressure gradient, and thermal pressure gradient gradually strengthen to counterbalance the inertial force. As shown in Figure 8, the inertial force is primarily balanced by the magnetic pressure gradient and the thermal pressure gradient. Due to the weak in-plane magnetic field, the contribution from magnetic tension force is negligible. These processes result in a weakening of the magnetic field within the vortices and a strengthening of the field between two vortices. Consequently, electrons undergo betatron heating or cooling.

4. Conclusions and Discussions

In this study, using a two-dimensional PIC simulation model, we investigated the mechanisms of electron energization during the evolution of the K-H instability based on the guiding-center theory. As the instability develops, vortices roll up and expand, distorting and stretching magnetic field lines, thereby converting flow kinetic energy into magnetic energy. During this phase, electron energization is primarily dominated by the betatron mechanism. Subsequently, the vortices gradually break up due to small-scale magnetic reconnection, returning magnetic energy to the plasma. The plasma becomes more turbulent, resulting in the formation of a broadened shear layer. The current breaks into smaller structures, and the original magnetic configuration is disrupted, reducing the contribution of the betatron term. At this stage, electron energization is mainly driven by the parallel electric field. Eventually, a larger vortex develops within the thickened shear layer, and the betatron mechanism again plays a dominant role. Throughout the entire process, the Fermi mechanism contributes minimally and may even have a cooling effect during the expansion of the vortices.

Our results indicate that electron energization is more likely to occur in the edge regions of the vortices, which is consistent with previous simulation studies (J. Goodwill et al. 2025). While numerous magnetic reconnection signatures are observed within the vortices (N. Ahmadi et al. 2025), their specific contribution to electron energization requires further quantitative assessment. Moreover, when a long numerical domain is used, vortex pairing processes dominate the system's dynamical evolution under different background magnetic field strengths (T. K. M. Nakamura & M. Fujimoto 2008; F. Califano et al. 2009; M. Faganello & F. Califano 2017). The structural characteristics of vortices merging events and whether they lead to significant energy gain remain important questions worthy of in-depth investigation.

Energetic electrons have been widely detected within flow vortices in space (F. Rieger 2019; C. M. Liu et al. 2025). Although the current simulations show that electron energization is mainly manifested as thermal enhancement without a significant suprathermal tail, further studies involving longer spatial and temporal scales and three-dimensional configurations are necessary to explore potential mechanisms for high-energy particle generation. Nevertheless, our simulations can reasonably explain certain observed structural features associated with vortex development, such as the formation of current sheets (S. Eriksson et al. 2016), temperature anisotropy (W. Li et al. 2016), and the locations and the mechanisms of electron energization. Our findings provide a reference

framework for explaining electron energization phenomena observed by the Magnetospheric Multiscale spacecraft and the Parker Solar Probe in high-shear regions. They also lay the foundation for understanding the microscale kinetic processes involved in solar wind–magnetosphere energy coupling.

Acknowledgments

This work was supported by the National Natural Science Foundation of China (NSFC) grant No. 42274196 and the Strategic Priority Research Program of Chinese Academy of Sciences grant No. XDB0560000.

ORCID iDs

Yuhang Yang https://orcid.org/0009-0008-6371-1594
San Lu https://orcid.org/0000-0003-2248-5072
Quanming Lu https://orcid.org/0000-0003-3041-2682
Ao Guo https://orcid.org/0000-0002-7625-7625
Wenya Li https://orcid.org/0000-0003-1920-2406

References

Ahmadi, N., Wilder, F. D., Ergun, R. E., et al. 2025, PhPl, 32, 022104
Arnold, H., Drake, J. F., Swisdak, M., et al. 2021, PhRvL, 126, 135101
Beresnyak, A., & Li, H. 2016, ApJ, 819, 90
Bucciantini, N., Olmi, B., & Zanna, L. D. 2020, JPhCS, 1623, 012002
Califano, F., Faganello, M., Pegoraro, F., & Valentini, F. 2009, NPGeo, 16, 1
Chandrasekhar, S. 1961, Hydrodynamic and Hydromagnetic Stability (Oxford Univ. Press)
Dahlin, J. T., Drake, J. F., & Swisdak, M. 2014, PhPl, 21, 092304
Dahlin, J. T., Drake, J. F., & Swisdak, M. 2016, PhPl, 23, 120704
Dahlin, J. T., Drake, J. F., & Swisdak, M. 2017, PhPl, 24, 092110
Derouillat, J., Beck, A., Pérez, F., et al. 2018, CoPhC, 222, 351
Eriksson, S., Lavraud, B., Wilder, V., et al. 2016, GeoRL, 43, 5606
Faganello, M., & Califano, F. 2017, JPlPh, 83, 535830601
Fromang, S., Leconte, J., & Heng, K. 2016, A&A, 591, A144
Goodwill, J., Adhikari, S., Li, X., et al. 2025, PhPl, 32, 052301
Guo, A., Lu, Q., Lu, S., Wang, S., & Wang, R. 2023, ApJ, 955, 14
Haggerty, C. C., Parashar, T. N., Matthaeus, W. H., et al. 2017, PhPl, 24, 102308
Hasegawa, H., Fujimoto, M., Phan, T.-D., et al. 2004, Natur, 430, 755
Hu, S., Lu, Q., Lu, S., & Wang, R. 2025, ApJ, 993, 66
Huang, C., Lu, Q., Guo, F., et al. 2015, GeoRL, 42, 7282
Huang, C., Lu, Q., Wang, R., et al. 2017, ApJ, 835, 245
Hwang, K.-J., Dokgo, K., Choi, E., et al. 2020, JGRA, 125, e2019JA027665
Jiang, K., Huang, S. Y., Lu, Q. M., Yuan, Z. G., & Xiong, Q. Y. 2025, GeoRL, 52, e2024GL111450
Johnson, J. R., Wing, S., & Delamere, P. A. 2014, SSRv, 184, 1
Karimabadi, H., Roytershteyn, V., Wan, M., et al. 2013, PhPl, 20, 012303
Kieokaew, R., Lavraud, B., Yang, Y., et al. 2021, A&A, 656, A12
Lapenta, G., Goldman, M., Newman, D. L., & Eriksson, S. 2022, ApJ, 940, 187
Li, W., André, M., Khotyaintsev, Y. V., et al. 2016, GeoRL, 43, 5635
Li, X., Guo, F., Li, H., Stanier, A., & Kilian, P. 2019, ApJ, 884, 118
Liu, C. M., Cao, J. B., Liu, Y. Y., et al. 2025, ApJ, 979, 96
Lu, Q., Huang, K., Guan, Y., Lu, S., & Wang, R. 2023, ApJ, 954, 146
Lu, Q., Wang, H., Huang, K., Wang, R., & Wang, S. 2018, PhPl, 25, 072126
Lu, S., Angelopoulos, V., Pritchett, P. L., et al. 2021, JGRA, 126, e2021JA029550
Lu, S., Guo, J., Lu, Q., et al. 2025, GeoRL, 52, e2025GL117084
Miura, A. 1984, JGRA, 89, 801
Miura, A., & Pritchett, P. L. 1982, JGRA, 87, 7431
Nakamura, T. K. M., Blasl, K. A., Hasegawa, H., et al. 2022, PhPl, 29, 012901
Nakamura, T. K. M., Eriksson, S., Hasegawa, H., et al. 2017, JGRA, 122, 11,505
Nakamura, T. K. M., & Fujimoto, M. 2008, PhRvL, 101, 165002
Nakamura, T. K. M., Hasegawa, H., Shinohara, I., & Fujimoto, M. 2011, JGRA, 116, A03227
Northrop, T. G. 1963, RvGeo, 1, 283
Nykyri, K., & Foullon, C. 2013, GeoRL, 40, 4154
Nykyri, K., & Otto, A. 2001, GeoRL, 28, 3565
Paouris, E., Stenborg, G., Linton, M. G., et al. 2024, ApJ, 964, 139
Paral, J., & Rankin, R. 2013, NatCo, 4, 1645
Pu, Z., & Kivelson, M. G. 1983, JGRA, 88, 841
Rieger, F. M., & Duffy, P. 2004, ApJ, 617, 155
Rieger, F. 2019, Galax, 7, 78
Settino, A., Nakamura, R., Blasl, K. A., et al. 2024, JGRA, 129, e2024JA032513
Steinvall, K., Richard, L., Fülöp, T., Hanebring, L., & Pusztai, I. 2025, JPlPh, 91, E90
Wan, M., Matthaeus, W. H., Karimabadi, H., et al. 2012, PhRvL, 109, 195001
Wang, C., & Belcher, J. W. 1998, JGRA, 103, 247
Wang, H., Lu, Q., Huang, C., & Wang, S. 2016, ApJ, 821, 84